Journal of
Manufacturing and Materials Processing

MDPI

Article

Investigating the Impact of Process Parameters on Bead Geometry in Laser Wire-Feed Metal Additive Manufacturing †

Mohammad Abuabiah [1,2,*], Tizia Charlotte Weidemann [3], Mahdi Amne Elahi [2], Bahaa Shaqour [1], Robin Day [3], Peter Plapper [2] and Thomas Bergs [4]

[1] Mechanical and Mechatronics Engineering Department, Faculty of Engineering and Information Technology, An-Najah National University, Nablus P.O. Box 7, Palestine; bahaa.shaqour@najah.edu
[2] Department of Engineering, University of Luxembourg, 6, Rue Coudenhove-Kalergi, L-1359 Luxembourg, Luxembourg; mahdi.amne.elahi@gmail.com (M.A.E.); peter.plapper@uni.lu (P.P.)
[3] Fraunhofer Institute for Production Technology IPT, Steinbachstraße 17, 52074 Aachen, Germany; tizia.weidemann@ipt.fraunhofer.de (T.C.W.); robin.day@ipt.fraunhofer.de (R.D.)
[4] Manufacturing Technology Institute MTI, RWTH Aachen University, Campus-Boulevard 30, 52074 Aachen, Germany; thomas.bergs@ipt.fraunhofer.de
* Correspondence: m.abuabiah@najah.edu
† This paper is an extended version of our paper published in Lasers in Manufacturing Conference—LiM, Munich, Germany, 26–29 June 2023.

Abstract: Laser wire-feed metal additive manufacturing (LWAM) is an innovative technology that shows many advantages compared with traditional manufacturing approaches. Despite these advantages, its industrial adoption is limited by complex parameter management and inconsistent process quality. To address these issues and improve geometric accuracy, this study explores how process parameters influence bead geometry. We conducted a parameter study varying laser power, wire feed rate, traverse speed, and welding angle. Using a full factorial design with a central composite design methodology, we assessed bead height and width. This allowed us to develop a model to estimate ideal process parameters. The findings offer a detailed analysis of parameter interactions and their effects on bead geometry, aiming to enhance geometric accuracy and process stability in LWAM. Moreover, we have evaluated the proposed process parameters from our developed model, which showed a significant enhancement to the overall quality. This was validated via printing a single layer and multi-layer structures. The quality of the final predicted sample using the proposed method was improved by 40% compared to the best sample produced for the Design of Experiment trials.

Keywords: laser wire-feed metal additive manufacturing; bead geometry; design of experiment; process optimization

Citation: Abuabiah, M.; Weidemann, T.C.; Elahi, M.A.; Shaqour, B.; Day, R.; Plapper, P.; Bergs, T. Investigating the Impact of Process Parameters on Bead Geometry in Laser Wire-Feed Metal Additive Manufacturing. *J. Manuf. Mater. Process.* **2024**, *8*, 204. https://doi.org/10.3390/jmmp8050204

Academic Editor: Shuo Yin

Received: 16 August 2024
Revised: 5 September 2024
Accepted: 10 September 2024
Published: 19 September 2024

1. Introduction

Laser wire-feed metal additive manufacturing (LWAM), also known as laser metal deposition with wire, is an advanced method that uses a laser beam to melt a metallic wire and apply it onto a substrate. The process involves continuously feeding material, such as a metal alloy, into the focal point of the laser beam. The heat from the laser causes the wire to liquefy and form a molten pool between the wire and the substrate plate, as illustrated in Figure 1. This continual supply of material enables precise deposition onto the target surface [1–5].

To provide a comprehensive understanding of the LWAM technology, Abuabiah et al. [6] emphasize the importance of key aspects of LWAM, including parametric modeling, monitoring systems, control algorithms, and path-planning approaches. LWAM offers several advantages over traditional manufacturing processes, it enables minimal material waste, provides versatile application possibilities, and exhibits improved metallurgical properties [7–11]. Despite these benefits, the broad industrial implementation of LWAM faces

challenges stemming from its complex nature and inherent process instability, particularly concerning the inconsistent bead geometry [3,8,12–15]. To overcome this limitation and achieve higher geometric precision, extensive parameter studies have been conducted in recent years within the directed energy deposition (DED) domain. These studies aim to identify the key influencing parameters and optimize their combinations to enhance bead geometry control and stability, thereby facilitating automation and series production.

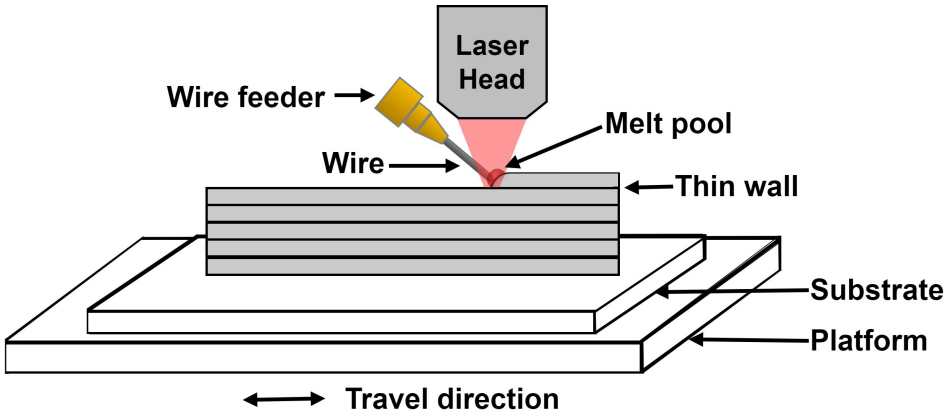

Figure 1. Schematic diagram of bead deposition in LWAM.

Dinovitzer et al. [16] examined the impact of process parameters on tungsten inert gas (TIG)-based wire arc additive manufacturing using Hastelloy X welding wire and stainless-steel 304 plates as the substrate. The study utilized the Taguchi method and analysis of variance (ANOVA) to analyze the effects of travel speed, wire feed rate, current, and argon flow rate on various responses such as bead shape, size, roughness, oxidation levels, melt-through depth, and microstructure. It was identified that travel speed and current were the most influential factors. The research also investigated different printing strategies involving multiple layers and concluded that there is no significant difference between printing layers in the same direction or alternating directions. Huang et al. [17] investigated the deposition of Al alloy 5A06 wire with a laser beam by producing single and multi-layered tracks. ANOVA analysis was used to determine the significance of main process parameters on the geometry characteristics of the deposited material. The study found a significant effect ofthe wire feeding direction and angle on the weight and dimension of the single tracks deposited.

On the other hand, past researchers solely investigated the effect of the bead's height or width in LWAM. Liu et al. [18] showed that laser power and traverse speed significantly affect the bead's width, while the wire feed rate and the interaction between laser power and traverse speed have less significant effects. On the other hand, the wire feeding rate and laser power have significant effects on the bead's height, with the interaction of laser power and wire feeding rate having a less significant effect. Moreover, Mok et al. [19] have shown that traverse speed significantly affects the bead's height more than laser power, while laser power affects the bead's width more significantly than traverse speed. In a related study, Moradi et al. [20] explored the influences of parameters on powder direct laser metal deposition of Inconel 718 using a full factorial design. They examined laser speed, powder feed rate, and scanning strategies as input variables, while geometrical dimensions, microhardness deviation, and wall stability served as process responses. ANOVA was employed to dissect the impact of process parameters on response variations, ultimately identifying optimal process conditions: a scanning speed of 2.5 mm/s, a powder feed rate of 28.52 g/min, and a unidirectional scanning pattern. Additionally, Ayed et al. [21] emphasized the importance of first-order process parameters in laser-wire deposition, namely wire feed speed, travel speed, and laser power. They successfully deposited titanium with power levels up to 5 kW and wire feed speeds of 5 m/min, ensuring process repeatability. However, initiating deposits sequentially, with the laser first and then wire feed, led to

issues such as molten titanium drops forming at the wire's end, rising by capillarity, and causing fusion with the contact tube. Furthermore, laser powers exceeding 3 kW resulted in the contact tube melting due to beam reflection, thus impeding wire deposition.

On the other hand, Mbodj et al. [22] have introduced a machine-learning regression algorithm aimed at predicting layer geometry in LWAM. They investigated the impact of deposition parameters on bead geometry through a neural-network analysis. Their research revealed the effective prediction of bead height, width, and ratio, while also exploring the influence of laser power, wire feed rate, and travel speed. Similarly, Liu, Brice, and Zhang [23] proposed a machine-learning-based material design framework, leveraging experimental data derived from LWAM of Ti-6Al-4V. Their dataset included various process variables and output characteristics, encompassing bead quality, shape, and microstructures. Data-driven machine-learning models were utilized to capture the intricate relationships between process parameters, geometry, and microstructure, visualizing these relationships through a 3D contour map. Additionally, Zapata et al. [24] directed their focus toward coaxial LWAM development, employing both aluminum and stainless-steel wire materials. Through regression analysis, they delved into the influence of process parameters on bead height and width. Their findings highlighted the suitability of a linear model in describing the correlation between process parameters and bead dimensions. Particularly, they identified the energy per unit length and speed ratio proportion as crucial factors for achieving defect-free processes.

The existing literature offers valuable insights into how various process parameters influence bead geometry in LWAM. However, a gap remains in understanding the combined effects of laser power, wire feed rate, traverse speed, and welding angle on bead deposition. Previous studies have largely focused on individual parameters or limited combinations, with minimal exploration of their interactions with bead characteristics such as height and width. This study addresses this gap by examining the collective impact of these parameters on a calculated quality index, rather than focusing solely on the bead's width or height. In this manuscript, we extend our previous work [25] by redesigning the Design of Experiments (DoE) using a full factorial design experiment with the central composite design method to systematically analyze parameter interactions and employ an advanced image processing technique for precise data measurement. By exploring a broad range of parameter combinations, we aim to provide a comprehensive understanding of their effects on bead geometry in the LWAM process.

Ensuring a stable deposition process is crucial for successful welding operations. The consistency and uniformity of the deposited part's geometry play a vital role in ensuring reliable outcomes. In this study, our primary aim is to analyze how various parameters affect the bead geometry during LWAM. To accomplish this goal, we conducted welding experiments, focusing on the deposition of single beads. During these experiments, we systematically adjusted the welding parameters for each bead and thoroughly examined their resulting geometry.

By carefully adjusting the parameters, our goal is to gain insights into their influence on the bead geometry. This investigation provides valuable knowledge about how different settings can impact the quality and consistency of the deposited material. Analyzing and understanding the relationship between these parameters and bead geometry is crucial for optimizing the LWAM process and achieving desirable outcomes.

We have organized the paper as follows. In Section 2, we describe the methodology employed in this study. This section includes the process of selecting key parameters (Section 2.1), the design of the experiment (Section 2.2), and a detailed overview of the experimental procedure and setup (Section 2.3). We then present the experimental measurements in Section 2.4 and conclude with a discussion on the quality model index for the deposited samples (Section 2.5). Section 3 provides the results and discussion, where we also provide the validation of the proposed model (Section 3.1). Finally, Section 4 presents the conclusions drawn from this work.

2. Methodology

2.1. Parameters Selection

In this study, we focused on four key parameters: laser power (PW), wire feed rate (W_f), traverse speed (T_s), and welding head angle (H_a). These parameters are pivotal variables often scrutinized due to their significant impact on the welding process [6]. Laser power directly influences heat input, thus affecting melt pool geometry and subsequently, bead geometry. Wire feed rate and traverse speed are closely intertwined with laser power, as adjustments in one invariably alter the others. These parameters dictate the volume of deposited wire, consequently influencing bead geometry.

In contrast, the welding head angle, or incident angle, has received minimal attention in LWAM studies. It is essential to distinguish it from the wire feeding angle, which describes the angle between the wire and the substrate plate. The incident angle refers to the angle between the laser and the substrate plate, as shown in Figure 2. In the standard experimental setup, the welding head is positioned so that the laser beam is perpendicular to the substrate, corresponding to a welding head angle defined as 0°, which we selected as the low value in our study. In our experimental setup, the laser and wire cannot be independently rotated as they are fixed together in the welding head. Thus, adjusting the welding head angle alters both the incident angle and wire feeding angle. Therefore, we refer to this angle as the welding head angle. Given its impact on heat flow, controlling the welding head angle can likely influence solidification and, consequently, geometry.

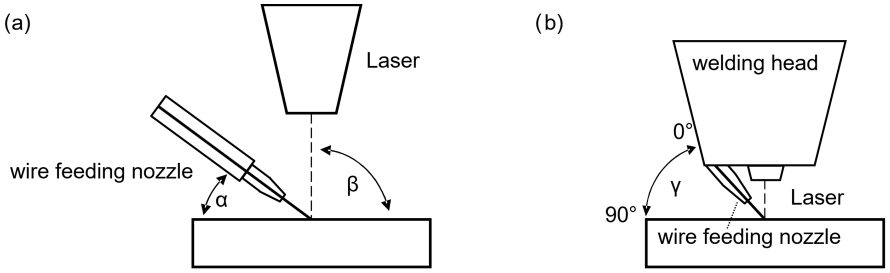

Figure 2. (**a**) Definition of wire feeding angle α and incident angle β [25]. (**b**) Experimental setup showing welding head angle γ.

2.2. Design of Experiment

The methodology employed in this study aimed to thoroughly investigate the effects of four different parameters, namely PW, W_f, T_s, and H_a, on the final product deposition in LWAM. To achieve comprehensive results with a limited number of experiments, a central composite design (CCD) experiment was chosen. This design is known for its efficiency in complex experimental setups, allowing researchers to assess multiple variables and their interactions simultaneously [26].

Specifically, the full-factorial design was adopted for this experiment. This design approach offers a two-level design with center points, allowing for a balanced exploration of the parameter space. The center points were run three times to ensure a more uniform estimate of the prediction variance across the entire design space. By incorporating center points, it becomes possible to detect potential curvature in the response surface and assess the influence of interactions between the parameters.

To minimize the impact of unmeasured and uncontrolled disturbances on the system's response, the actual experiments were conducted in random order. This randomized order of experiments was achieved using the Fisher-Yates algorithm, ensuring that any potential biases or confounding effects were evenly distributed.

Since four parameters are under investigation, the factorial design employed yields a total of 31 experiments. This calculation considers the combinations of parameter settings across the two levels of each parameter, resulting in 16 factorial-cube points. Additionally, the three runs of the 7 center points in the cube are included with 8 axial points, bringing the total number of experiments to 31. By systematically varying the parameter settings

in these experiments, we can effectively explore and analyze the individual effects of each parameter as well as their potential interactions on the final product deposition. This comprehensive approach allows for a thorough understanding of how each parameter contributes to the observed outcomes.

The general strategy for determining the parameter values is to choose low and high values representative of normal operation, as provided in Table 1. More specifically, Inconel 718 was selected as the wire material, leading to a range of laser power from 1800 W to 2500 W. The high and low values of the wire feed rate and the traverse speed were set to 1000 mm/min and 1600 mm/min, respectively. A welding head angle of 0° was chosen as the low value, representing the usual experimental setup with no change in the angle. To explore the effect of welding head angle while ensuring the process still functions, a small variation was applied, setting the high value to 10°.

Table 1. Parameter ranges for the investigation of the parameter influence on the bead geometry.

	Minimal Value	**Maximal Value**
PW [W]	1800	2500
W_f [mm/min]	1000	1600
T_s [mm/min]	1000	1600
H_a [°]	0	10

Statistical analysis was conducted using Minitab® 21.4. A response surface design of experiment analysis was used to set up the experiment. The software was utilized to establish a central composite design with a randomized experiment as shown in Table 2. Where StdOrder refers to the standard order, which is the non-randomized sequence of the runs, PtType denotes the point type, where 0 indicates a center point run, and ±1 represents a corner point.

Table 2. Parameter list of the design of the experiment.

StdOrder	**RunOrder**	**PtType**	PW	W_f	T_s	H_a
23	1	−1	2150	1300	1300	0
1	2	1	1975	1150	1150	2.5
17	3	−1	1800	1300	1300	5
11	4	1	1975	1450	1150	7.5
21	5	−1	2150	1300	1000	5
30	6	0	2150	1300	1300	5
14	7	1	2325	1150	1450	7.5
28	8	0	2150	1300	1300	5
25	9	0	2150	1300	1300	5
24	10	−1	2150	1300	1300	10
29	11	0	2150	1300	1300	5
3	12	1	1975	1450	1150	2.5
10	13	1	2325	1150	1150	7.5
22	14	−1	2150	1300	1600	5
20	15	−1	2150	1600	1300	5
27	16	0	2150	1300	1300	5
19	17	−1	2150	1000	1300	5
4	18	1	2325	1450	1150	2.5
16	19	1	2325	1450	1450	7.5
7	20	1	1975	1450	1450	2.5
6	21	1	2325	1150	1450	2.5
2	22	1	2325	1150	1150	2.5
9	23	1	1975	1150	1150	7.5
5	24	1	1975	1150	1450	2.5
26	25	0	2150	1300	1300	5
13	26	1	1975	1150	1450	7.5
18	27	−1	2500	1300	1300	5
8	28	1	2325	1450	1450	2.5
12	29	1	2325	1450	1150	7.5
31	30	0	2150	1300	1300	5
15	31	1	1975	1450	1450	7.5

2.3. Experimental Procedure and Setup

The experiments were carried out at the Fraunhofer IPT using the "Multi-Technology Robot System for Adaptive Manufacturing" (MIRA). The MIRA robot cell, shown in Figure 3, includes an ABB IRB 6660 industrial robot arm with the custom-built welding head "LMD-W-20-L". This welding head combines a lateral wire feed, a shielding gas supply and the optical system of the laser in one unit. The wire feeding system is positioned at an angle of 20 degrees to the optical axis. Next to the optical system, the nozzle for the shielding gas Argon is located. To feed the wire, the "Master-Feeder-System V3" (MFS-V3) from Abicor Binzel is used. The "Laserline LDF 4500-30 VGP" diode laser serves as a laser source and has a maximum output power of 4500 W.

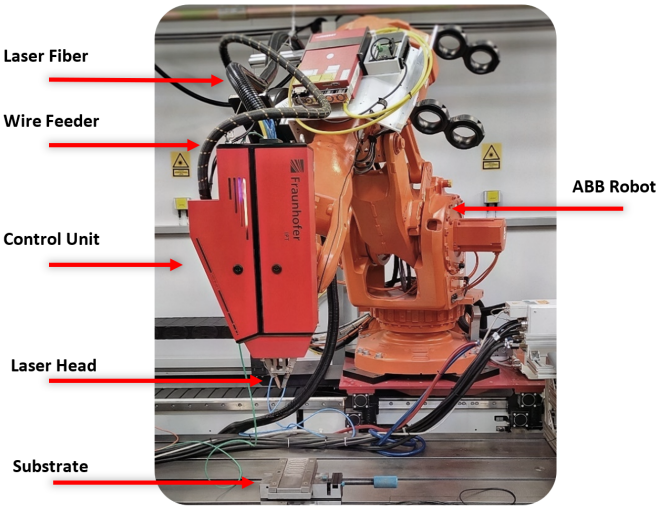

Figure 3. Experimental setup of the laser metal deposition with wire at Fraunhofer IPT.

For the bead deposition, Inconel 718 wire material with a diameter of 1.2 mm was used as filler material. The laser spot diameter was set at 2.1 mm and was not changed during the experiments. The beads were deposited on a substrate plate of size 200 mm × 80 mm × 15 mm of 1.0570 steel. We carefully executed each parameter set, which involved depositing a single bead that spanned a length of 6 cm. We captured optical observations of multiple individual deposits generated by LWAM and presented them in Figure 4, where the laser spot diameter was set at 2.1 mm.

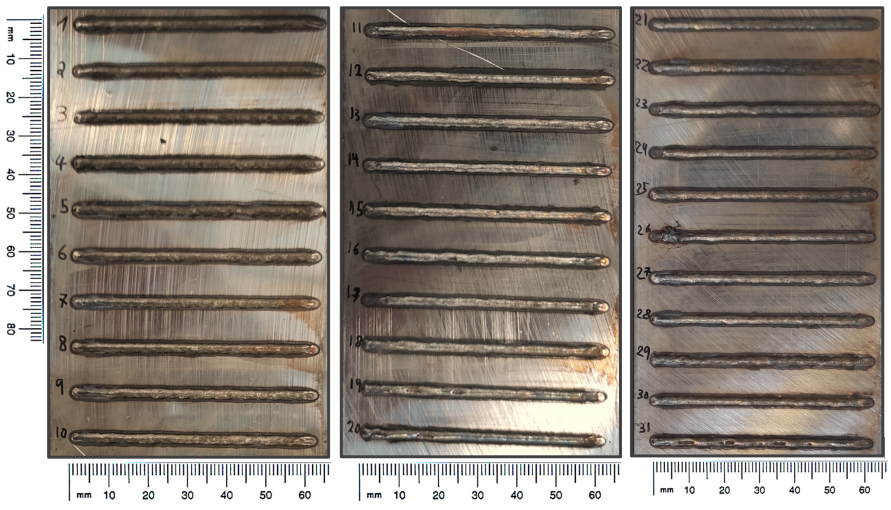

Figure 4. Top view image of the deposition samples.

2.4. Experimental Measurements

In LWAM, the width (W) and height (H) of the deposited bead are critical parameters that significantly influence the accuracy and quality of the final product. The reliance on the width and height measurements to evaluate the deposited bead quality has been used in many previously published works [18,25,27]. The bead width determines the horizontal extent of the deposited material, impacting the bead's overall dimensional consistency and adherence to the design specifications. A consistent width is essential for ensuring uniform layer deposition and achieving the desired geometry, particularly in multi-layer builds. The bead height, on the other hand, reflects the vertical deposition and affects the layer bonding and structural integrity of the preceding layers. Variations in height can lead to uneven surfaces and poor inter-layer adhesion, compromising the mechanical properties and visual quality of the final product. Figure 5 illustrates the height and the width of the bead dimensions. Accurate measurement and control of both width and height are crucial for optimizing deposition quality, ensuring that the manufactured components meet the required specifications and performance standards.

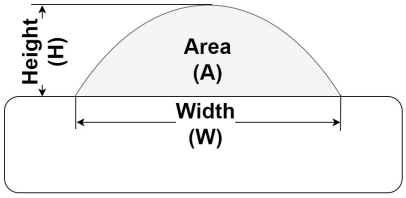

Figure 5. Schematic diagram of a single bead's height, width, and area dimensions in the cross-sectional view.

The beads were separated for subsequent metallographic examination. To ensure precise width measurements, we conducted 175 measurements for each deposition along its length using the Image Processing "Image Segmenter app" in MATLAB®, version R2020a.

For simplicity, Sample No. 2 will be used for the analysis and calculation in this section, without losing generality. Initially, each sample was converted to a high-resolution black and white image, exemplified in Figure 6a for Sample No. 2, capturing intricate details of the deposited sample. Subsequently, we delineated a region of interest (ROI) around the sample using local graph cut segmentation. Morphology operations were then employed to refine the boundary of each sample using a close-make operation, as shown in Figure 6b. Finally, a MATLAB script was developed to automatically calculate the width of each sample at 175 locations in millimeters, as illustrated in Figure 6c.

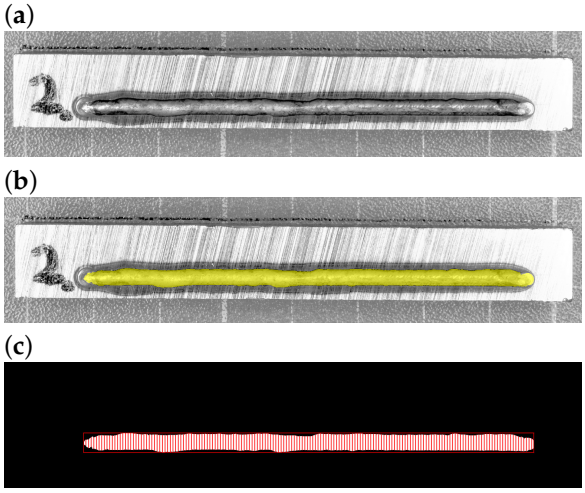

Figure 6. (**a**) High-resolution black and white image of Sample No. 2. (**b**) Region of interest delineation using local graph cut segmentation and morphology. (**c**) Automatic width calculation at 175 locations.

To determine the height profile, we examined the longitudinal sections of each sample using a Leica DM 4000 M optical microscope. The bead height was measured at 175 evenly spaced intervals along the entire length of the deposition, from start to finish, as illustrated in Figure 7.

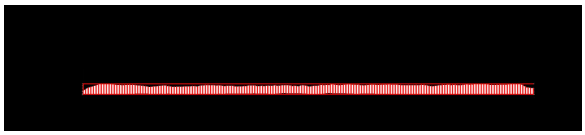

Figure 7. Cross-section of bead height for Sample No. 2, with calculations at 175 locations.

We also calculated the deposition area (A) for each width and height measurement for each sample by simplifying the bead cross-sections to half-ovals (see Figure 5), using the following equation:

$$A = \frac{\pi \times \text{Width} \times \text{Height}}{4} \quad (1)$$

The width, height, and area profiles of Sample No. 2 were measured along its 62 mm length, as illustrated in Figure 8. These measurements were taken at 175 evenly spaced intervals, each representing a segment of the sample's total length. At each interval, the width and height were recorded in millimeters, and the area was calculated in square millimeters (mm^2), providing detailed insights into the sample's physical dimensions. Although Figure 8 specifically depicts the profiles of Sample No. 2, this measurement process was consistently applied to all 31 samples, ensuring a comprehensive and precise analysis.

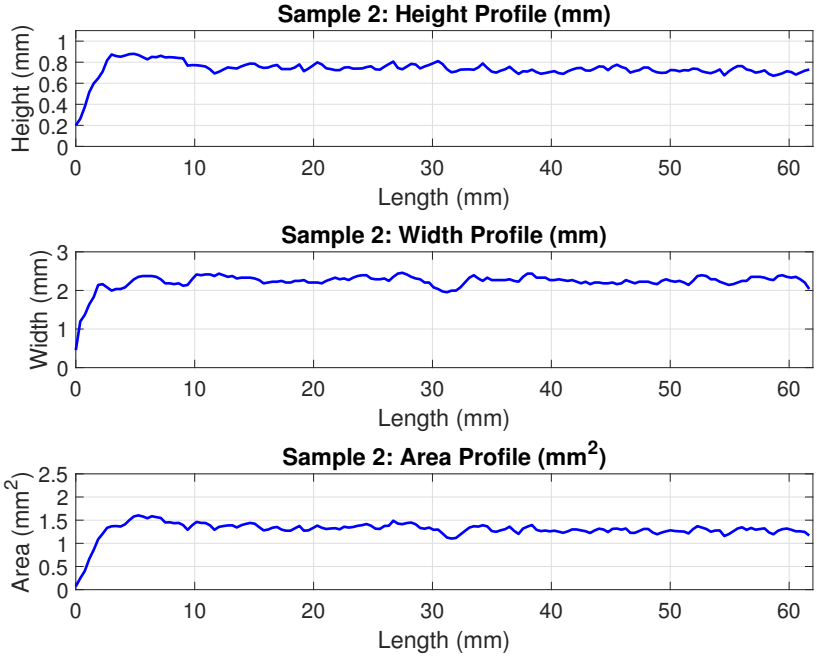

Figure 8. Profiles of Sample No. 2 showing width, height, and area measurements along its length.

The volume of each deposited bead was calculated from the measurements of the half-oval areas using numerical integration. Since the measurements were taken at regular intervals along the deposition, the trapezoidal rule was applied to approximate the total volume:

$$V \approx \sum_{i=1}^{n-1} \frac{A(i) + A(i+1)}{2} \times \Delta x \quad (2)$$

where $A(i)$ is the area of each section in the deposited bead calculated in Equation (1), Δx is the distance between consecutive measurements, and $n = 175$ is the number of measurements.

To evaluate the consistency of the deposition process, we calculated the standard deviation generated from the variation among the 175 volume segments for each bead, which provides insight into variations in both height and width. This metric helps us understand the consistency of the deposition process.

For comparative analysis and optimization, we standardized both the volume and its standard deviation for each sample on a scale from 0 to 1. This standardization involved normalizing the measurements using the maximum and minimum values observed across all samples, focusing on both the volume and standard deviation metrics. The standardization step is explained in the following section.

2.5. Sample Quality

In this subsection, we developed a quality score to identify the optimal deposition parameters based on the total volume of the deposition (V). The quality score identifies the optimal deposition parameters, defining the ideal conditions as those with the largest bead volume and the smallest standard deviation. To balance the importance of both deposition quantity and consistency, we assigned equal weight—50% each—to the volume and its standard deviation. This approach ensures that neither factor disproportionately affects the model's outcome. The standardized quality score values, ranging from 0% to 100%, represent the effectiveness of each deposition setting in achieving both high volume and low variability.

For self-consistency in the manuscript, here is a comprehensive sample calculation of the proposed quality score using Sample No. 2. For Sample No. 2, the bead's volume is 80.56 mm^3, and the standard deviation among its volume segments is 0.06. We also need the minimum and maximum values for normalization. The minimum and maximum volume values across all samples are 97.96 mm^3 and 50.76 mm^3, respectively. The minimum and maximum standard deviations calculated for volume segments for the deposited beads are 0.03 and 0.13, respectively. First, we standardize the bead's volume. The normalization formula for the volume is:

$$\text{Normalized Volume} = \frac{V - \text{Min V}}{\text{Max V} - \text{Min V}} \approx 0.63 \tag{3}$$

This result means that the normalized volume for Sample No. 2 is approximately 0.63 on a scale from 0 to 1. Next, we standardize the standard deviation using the following normalization formula:

$$\text{Normalized STD (V)} = \frac{\text{STD (V)} - \text{Min STD (V)}}{\text{Max STD (V)} - \text{Min STD (V)}} \approx 0.67 \tag{4}$$

This result means that the normalized standard deviation for Sample No. 2 is approximately 0.67 on a scale from 0 to 1. To combine these normalized values into a quality score, we use the following formula:

$$\text{Quality Score} = 0.5 \times \text{Normalized Volume} + 0.5 \times (1 - \text{Normalized STD (V)}) \tag{5}$$

Therefore, the standardized quality score for Sample No. 2 is 0.65, or 65%. This score reflects the sample's performance in terms of both the size of the deposition (volume) and its consistency (standard deviation), with a higher score indicating better quality.

3. Results and Discussion

In this section, we present a comprehensive analysis of the bead deposition process in LWAM, focusing on volume calculations, standardization, and optimization of deposition parameters. Our study utilized a detailed statistical approach to evaluate the quality and consistency of bead depositions across 31 samples.

All samples' average width, height, and area are shown in Figure 9. Furthermore, Figure 10 presents the computed volume and its standard deviation for the deposited samples. By examining these measurements, we can identify variations in the deposition process and detect potential areas of irregularity or defect, which are crucial for assessing the structural integrity and performance of the samples. This thorough examination enhances our understanding of the LWAM process and its impact on the final product's quality.

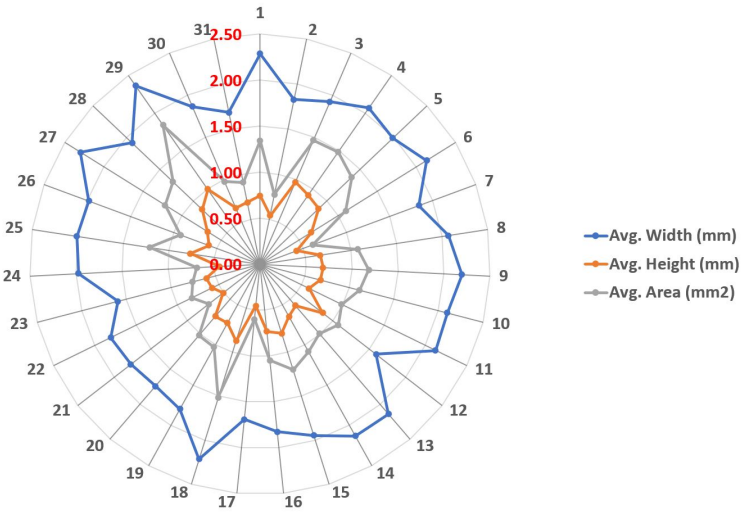

Figure 9. Radar chart showing the average width, height, and area of the 31 samples.

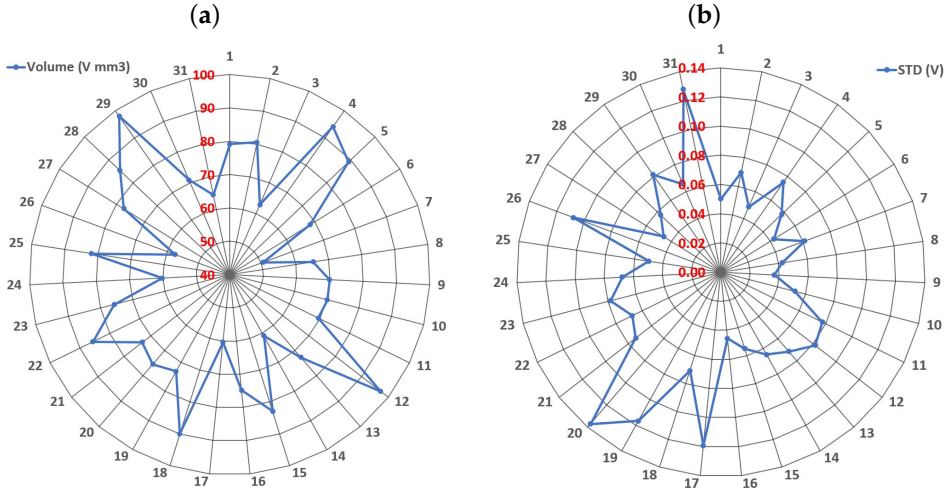

Figure 10. Radar chart displaying the sample's volume (**a**) and its volume standard deviation (**b**).

Figure 11 illustrates the radar chart displaying the quality score values as percentages for each of the 31 deposited samples. This chart visually distinguishes between high and low-quality samples, where samples such as 1, 4, 5, 28, and 29 are identified as exhibiting consistent quality, while samples 17, 26, and 31 are categorized as the worst. These findings are consistent with the detailed measurement analysis conducted. For instance, Sample No. 5, with a high-quality score of 80%, exhibits a profile characterized by steady width, height, and area measurements, indicating good-quality deposition, as shown in Figure 12.

Conversely, Sample No. 31, with a low-quality score of 19%, as illustrated in Figure 13, displays numerous holes within the deposit and fluctuating values in width, height, and area. This discrepancy correlates with its lower quality score. The consistency between the radar chart and measurement profiles verifies the accuracy of the quality assessment.

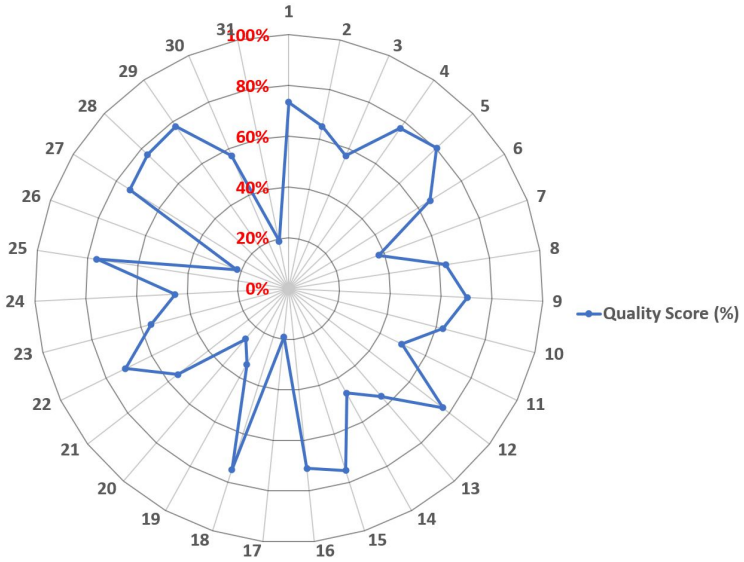

Figure 11. Radar chart of the quality score values in percentage for each deposited sample.

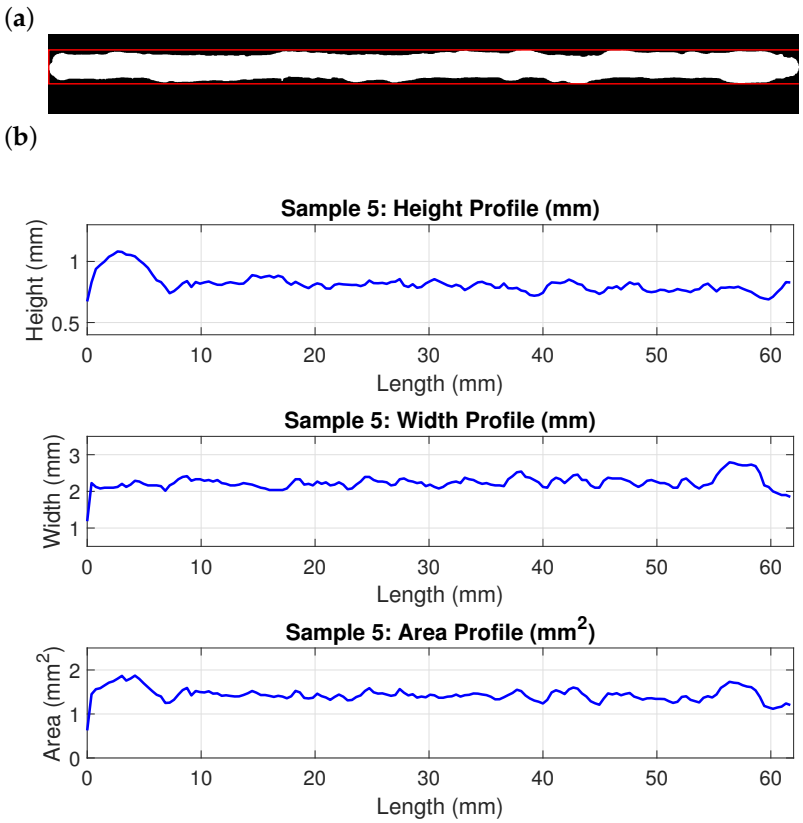

Figure 12. (**a**) Top view image mask for Sample No. 5 deposition. (**b**) Profiles of Sample No. 5 showing width, height, and area measurements along its length.

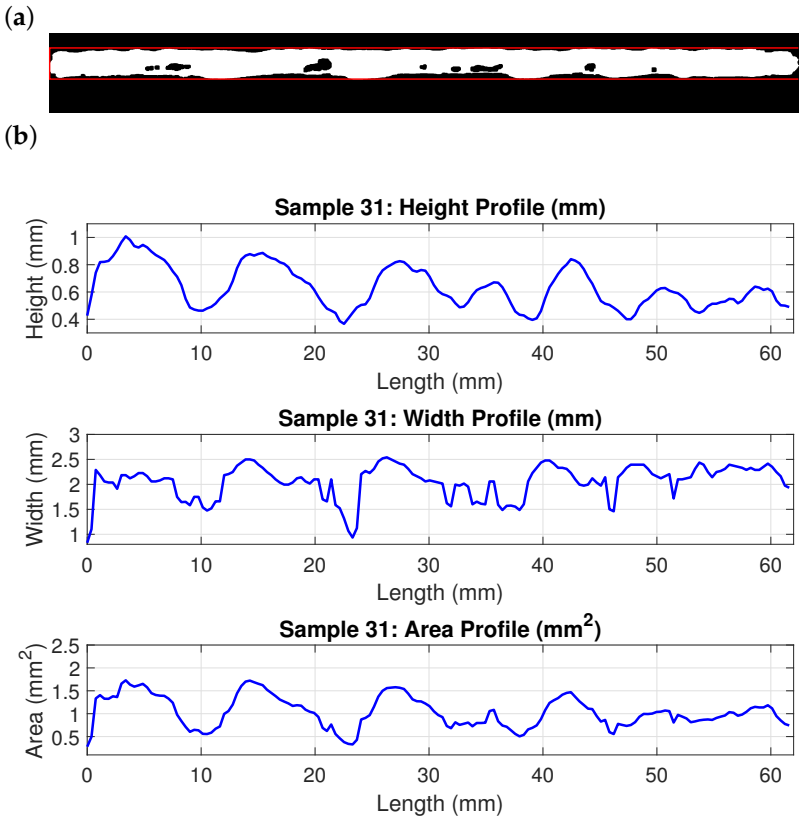

Figure 13. (**a**) Top view image mask for Sample No. 31 deposition. (**b**) Profiles of Sample No. 31 showing width, height, and area measurements along its length.

The analysis of variance (ANOVA) results, presented in Table 3, provide insights into how different parameters affect the quality model. Due to the complexity of the model, the significance level was set to $\alpha = 0.1$. The model's f-value of 10.60 ($p < 0.001$) indicates that the variables significantly impact deposition quality.

Table 3. Analysis of variance.

Source	DF	Adj SS	Adj MS	f-Value	p-Value
Model	6	0.77883	0.129805	10.6	0
Linear	4	0.64953	0.162382	13.26	0
PW	1	0.07129	0.071286	5.82	0.024
W_f	1	0.1146	0.114603	9.36	0.005
T_s	1	0.39	0.390005	31.84	0
H_a	1	0.07363	0.073634	6.01	0.022
Square	1	0.08195	0.081951	6.69	0.016
$W_f \times W_f$	1	0.08195	0.081951	6.69	0.016
2-Way Interaction	1	0.04735	0.047354	3.87	0.061
$PW \times T_s$	1	0.04735	0.047354	3.87	0.061
Error	24	0.29394	0.012248		
Lack-of-Fit	18	0.24355	0.013531	1.61	0.289
Pure Error	6	0.05039	0.008398		
Total	30	1.07278			

It is important to note that in constructing the model presented in Table 3, we initially started with a full quadratic model that included all single, linear, and quadratic terms based on the defined DoE. However, following statistical analysis and a review of the ANOVA table, we employed a backward elimination process to remove non-significant parameters—those with a P-value higher than the significance level. Consequently, certain quadratic terms like $PW \times PW$ and $T_s \times T_s$ were excluded from the final model, as their coefficients were very small, making these terms negligible in predicting the outcomes.

The linear effects show significant contributions from several parameters. The parameter PW has an f-value of 5.82 with a p-value of 0.024, indicating its significant influence on the model. Similarly, the parameter W_f exhibits an f-value of 9.36 and a p-value of 0.005, demonstrating a notable effect. The parameter T_s is particularly influential, with an f-value of 31.84 and a highly significant p-value of less than 0.001. Additionally, H_a shows a significant contribution with an f-value of 6.01 and a p-value of 0.022.

The square effects demonstrated significance for the parameter $W_f \times W_f$, with an f-value of 6.69 and a p-value of 0.016. Furthermore, the two-way interaction between PW and T_s approached significance, as indicated by an f-value of 3.87 and a p-value of 0.061. Finally, the error analysis further confirms the robustness of the model, as indicated by the non-significant lack-of-fit ($p = 0.289$), suggesting that the model adequately captures the variability in the data.

The relationship between the process parameters and the response variable, which we will refer to as the quality index (R), is described by the following regression equation in uncoded units:

$$\begin{aligned} R =& 2.40 - 0.00238PW + 0.00656W_f - 0.00531T_s - 0.02216H_a \\ & - 0.000002W_f \times W_f + 0.000002PW \times T_s \end{aligned} \quad (6)$$

This equation shows that increasing the (W_f) positively affects the quality model. Conversely, increasing the (T_s) and the (H_a) negatively impacts the quality model, as reflected by their negative coefficients. Additionally, the coefficient for laser power (PW) is negative, suggesting that higher laser power reduces the quality of the model. The term for the square of the wire feed rate (W_f^2) also contributes negatively, while the interaction term between (PW) and (T_s) has a small positive effect.

Furthermore, Figure 14 presents the Pareto chart of the standardized effects with $\alpha = 0.1$. In this figure, PW is denoted as Factor A, W_f as Factor B, T_s as Factor C, and H_a as Factor D. The Pareto chart illustrates that the standardized effect of Factor C (travel speed) is the largest, indicating its significant influence on the quality model. In contrast, the effects of Factor B squared ($W_f{}^2$), Factor D (head angle), and Factor A (power) are almost the same and less significant. The interaction effect between Factors A and C (AC) is shown to be even smaller.

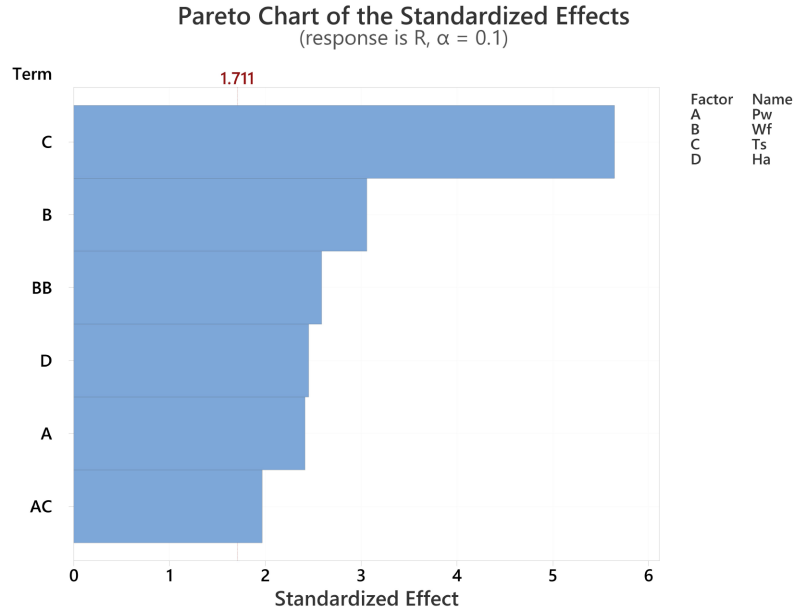

Figure 14. Pareto chart of standardized effects ($\alpha = 0.1$).

Figure 15 displays the residual plots for the response variable R, including a normal probability plot, a plot of residuals versus fits, a histogram of residuals versus frequency, and a plot of residuals versus observation order. The normal probability plot suggests that the residuals are approximately normally distributed, as they closely follow the reference line. The plot of residuals versus fits shows a random scatter, indicating that there are no obvious patterns and that the model's assumptions are valid. The histogram of residuals further supports the normality of the residuals, while the plot of residuals versus order suggests that there is no significant time-related correlation in the data. Overall, these residual plots confirm the adequacy and reliability of the regression model.

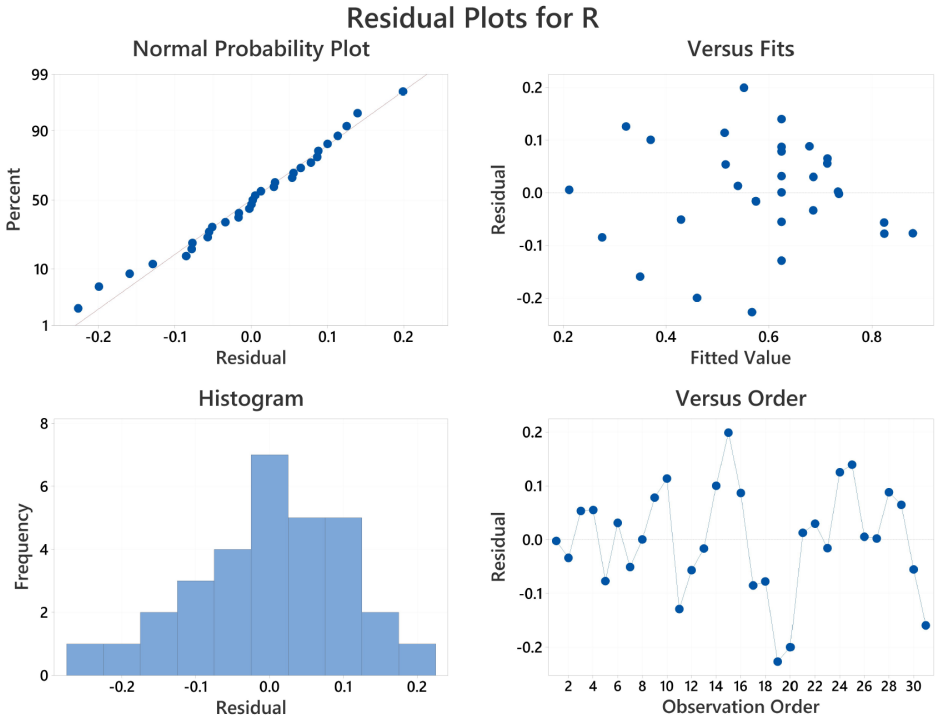

Figure 15. Residual plots for Quality Index R.

3.1. Model Validation

In this section, we extended the statistical analysis of the defined DoE model. With the regression model covering all significant process parameters, we implemented the response optimizer to determine the optimal process parameters for a desired quality score. In this case, the quality score was set to the maximum value experimentally achievable for the given setup. This resulted in multiple solutions for the optimum process parameters. Although all these solutions are statistically valid, some lead to process instability and inconsistent deposition due to the physical limitations of the setup. To address this, the power (PW) was fixed at 1800 W, limiting the options based on prior experiments. As a result, the response optimizer constrained W_f to 1533, T_s to 1145, and H_a to 0. Using these parameters, a final sample was prepared and deposited, as shown in Figure 16.

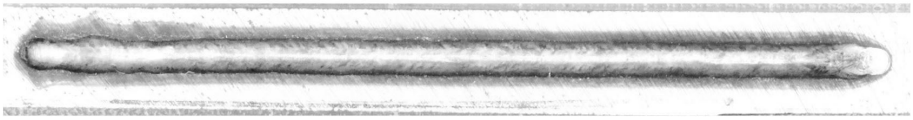

Figure 16. Final deposited bead: The image shows the bead deposited with the optimized parameters.

The resulting bead exhibited no irregularities and displayed an even surface, as depicted in Figure 16. The height and width profiles of this sample, obtained using the

same image processing technique described in the methodology section, are shown in Figure 17. The final deposited bead achieved a quality score value of 1.124, significantly surpassing the previous 31 bead depositions. This value shows an improvement of 491% and 40% when compared with the worst (Sample No. 31) and the best (Sample No. 5) samples, respectively. Moreover, the validation sample shows an increase of 73% and 25% in volume and a decrease of 69% and 30% in the standard deviation when compared with the worst (Sample No. 31) and the best (Sample No. 5) samples, respectively. This result demonstrates the effectiveness of our approach in achieving optimal deposition with high volume and consistency, confirming the model's predictive capability and robustness. The optimal parameters lead to a significant improvement in the quality score value, reflecting the model's ability to guide process optimization effectively.

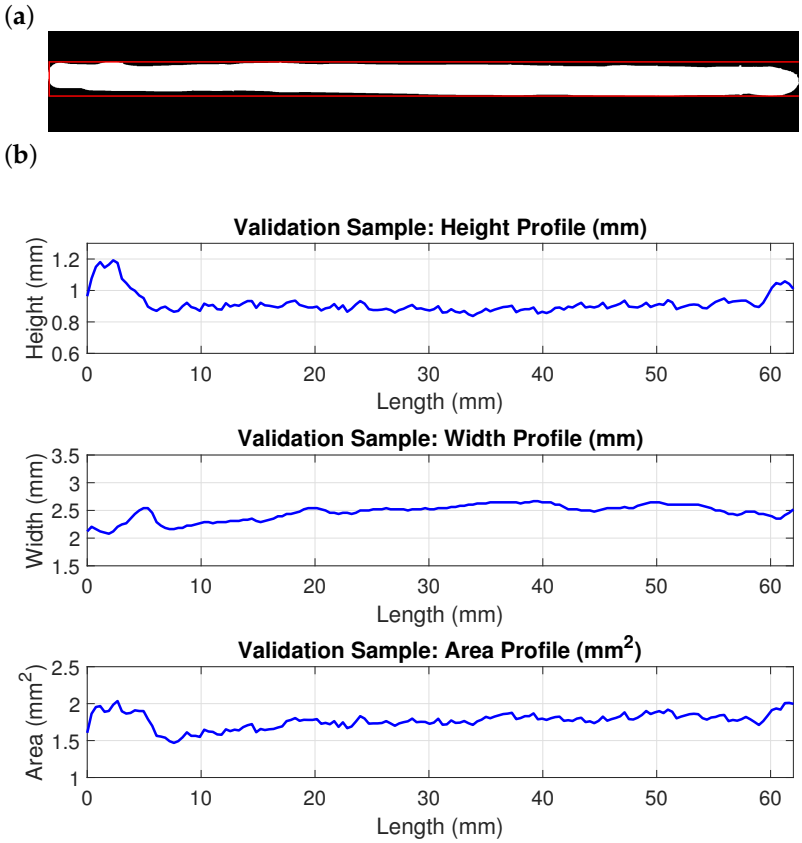

Figure 17. (**a**) Top view image mask for the validation sample deposition. (**b**) Profiles of the validation sample showing width, height, and area measurements along its 62 mm length.

Further validation of the model involved depositing geometry samples using the optimized parameters. Figure 18a presents microscope images of a sample's cross-sections, consisting of three layers of deposition, while Figure 18b depicts a six-layer deposition. Both samples exhibit regular geometry with a semicircular shape in the top layer. The bonding between layers and the substrate is flawless, with no visible defects or porosity. These observations confirm that the model is effective for depositing volumetric structures and achieving high-quality deposition without defects.

This additional test demonstrates that the model can perform well in depositing multi-layered structures, not just single-layer deposits. Although these results are promising, they primarily serve to validate that the obtained model can produce accurate geometries. Further work and comprehensive analysis, including the deposition of larger structures and mechanical testing of samples, are necessary to fully assess the model's applicability. However, such investigations are beyond the scope of this paper.

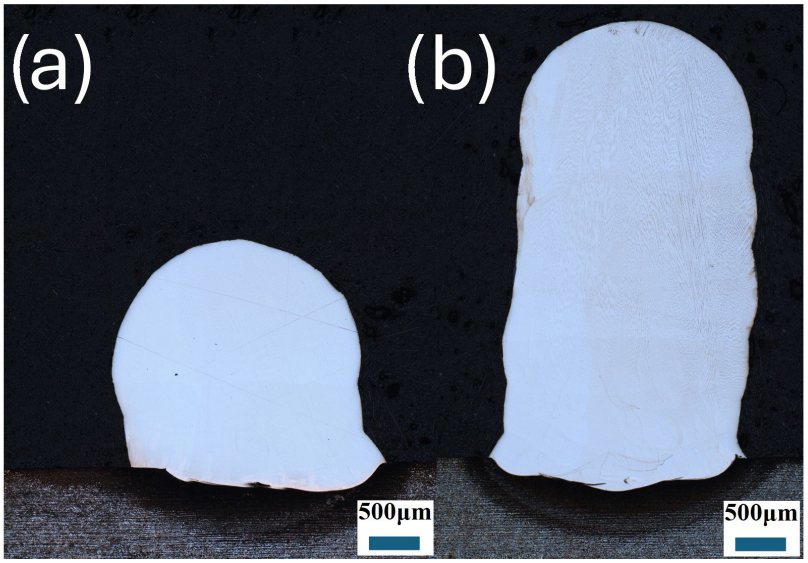

Figure 18. (**a**) Microscope image of a three-layer deposited sample. (**b**) Microscope image of a six-layer deposited sample.

4. Conclusions

This study presents a comprehensive evaluation of the LWAM process, focusing on optimizing deposition parameters and improving bead quality using a detailed statistical approach. A novel analytical method is included, incorporating 175 measurements of the width and height along each specimen. The research developed a robust quality model that ranks the quality of 31 deposited samples, identifying travel speed as the most significant factor affecting deposition quality, followed by wire feed rate, power, and head angle.

Key findings indicate that increasing the wire feed rate improves quality, while higher travel speed and head angle decrease it. The model's validation showed a significant improvement in bead quality, with a 491% improvement over the worst sample and a 40% improvement over the best sample. The successful deposition of multi-layered structures confirmed the model's applicability to complex geometries. This study lays a strong foundation for future research, suggesting larger-scale testing and mechanical evaluation to further establish the model's effectiveness in optimizing LWAM parameters.

Author Contributions: Conceptualization, methodology, investigation, and original draft preparation, M.A., T.C.W., M.A.E. and B.S.; review and editing, M.A., T.C.W., M.A.E., B.S., P.P. and T.B.; supervision, T.B., P.P. and R.D.; project administration and funding acquisition, P.P. and M.A. All authors have read and agreed to the published version of the manuscript.

Funding: This research was funded by the BALSAM project, which is part of the EU Framework Programme for Research and Innovation within Horizon Europe—Marie Sklodowska-Curie Postdoctoral Fellowships 2021, under grant agreement No. 101064640.

Data Availability Statement: The data supporting the reported results are available on ZENODO and can be accessed as an Excel file. This file provides detailed data regarding the design of experiments (DoE) for the research project investigating the impact of process parameters on bead geometry in laser wire-feed metal additive manufacturing, conducted under the BALSAM project. The Excel file can be found using the following link: https://zenodo.org/records/13332919, accessed on 15 August 2024.

Acknowledgments: We would like to thank Fylyp Butenko for his assistance with microscopy imaging and sample measurements. We also dedicate this work to the memory of Peter Plapper, whose unwavering support, guidance, and supervision made this project possible.

Conflicts of Interest: The authors declare no conflicts of interest.

References

1. Craeghs, T.; Bechmann, F.; Berumen, S.; Kruth, J.P. Feedback control of Layerwise Laser Melting using optical sensors. *Phys. Procedia* **2010**, *5*, 505–514. [CrossRef]
2. Akbari, M.; Ding, Y.; Kovacevic, R. Process development for a robotized laser wire additive manufacturing. In Proceedings of the International Manufacturing Science and Engineering Conference, Zhuhai, China, 11–12 March 2017; American Society of Mechanical Engineers: New York, NY, USA, 2017; Volume 50732, p. V002T01A015.
3. Abadi, S.N.R.; Mi, Y.; Kisielewicz, A.; Sikström, F.; Choquet, I. Influence of laser-wire interaction on heat and metal transfer in directed energy deposition. *Int. J. Heat Mass Transf.* **2023**, *205*, 123894. [CrossRef]
4. Ma, L.; Liu, Z.; Feng, C.; Zhang, B.; Pang, M.; Feng, Q.; Wang, Y. Investigation on Forming Process and Product Properties of Laser Wire-Feed Additive Manufacturing for High-Quality Metal Thin-Walled Parts. *J. Mater. Eng. Perform.* **2024**, *33*. [CrossRef]
5. Assad, A.; Bevans, B.D.; Potter, W.; Rao, P.; Cormier, D.; Deschamps, F.; Hamilton, J.D.; Rivero, I.V. Process mapping and anomaly detection in laser wire directed energy deposition additive manufacturing using in-situ imaging and process-aware machine learning. *Mater. Des.* **2024**, *245*, 113281. [CrossRef]
6. Abuabiah, M.; Mbodj, N.G.; Shaqour, B.; Herzallah, L.; Juaidi, A.; Abdallah, R.; Plapper, P. Advancements in laser wire-feed metal Additive Manufacturing: A brief review. *Materials* **2023**, *16*, 2030. [CrossRef]
7. Ding, D.; Pan, Z.; Cuiuri, D.; Li, H. Wire-feed additive manufacturing of metal components: Technologies, developments and future interests. *Int. J. Adv. Manuf. Technol.* **2015**, *81*, 465–481. [CrossRef]
8. Xia, C.; Pan, Z.; Polden, J.; Li, H.; Xu, Y.; Chen, S.; Zhang, Y. A review on wire arc additive manufacturing: Monitoring, control and a framework of automated system. *J. Manuf. Syst.* **2020**, *57*, 31–45. [CrossRef]
9. Casalino, G.; Karamimoghadam, M.; Contuzzi, N. Metal wire additive manufacturing: A comparison between arc laser and laser/arc heat sources. *Inventions* **2023**, *8*, 52. [CrossRef]
10. Tebianian, M.; Aghaie, S.; Razavi Jafari, N.S.; Elmi Hosseini, S.R.; Pereira, A.B.; Fernandes, F.A.; Farbakhti, M.; Chen, C.; Huo, Y. A Review of the Metal Additive Manufacturing Processes. *Materials* **2023**, *16*, 7514. [CrossRef]
11. Ghanadi, N.; Pasebani, S. A Review on Wire-Laser Directed Energy Deposition: Parameter Control, Process Stability, and Future Research Paths. *J. Manuf. Mater. Process.* **2024**, *8*, 84. [CrossRef]
12. Du, F.; Zhu, J.; Ding, X.; Zhang, Q.; Ma, H.; Yang, J.; Cao, H.; Ling, Z.; Wang, G.; Duan, X.; et al. Dimensional characteristics of Ti-6Al-4V thin-walled parts prepared by wire-based multi-laser additive manufacturing in vacuum. *Rapid Prototyp. J.* **2019**, *25*, 849–856. [CrossRef]
13. Roberts, M.; Xia, M.; Kennedy, A. Data-driven Process Parameter Optimisation for Laser Wire Metal Additive Manufacturing. In Proceedings of the 2022 27th International Conference on Automation and Computing (ICAC), Bristol, UK, 1–3 September 2022; IEEE: New York, NY, USA, 2022; pp. 1–6.
14. Jin, H.; Zhou, J. Experimental study and parameter optimization of laser wire additive manufacturing of titanium alloy. *J. Laser Appl.* **2024**, *36*, 032025. [CrossRef]
15. Zhu, S.; Nakahara, Y.; Yamamoto, M.; Shinozaki, K.; Aono, H.; Ejima, R. Additive manufacturing phenomena of various wires using a hot-wire and diode laser. *Weld. World* **2022**, *66*, 1315–1327. [CrossRef]
16. Dinovitzer, M.; Chen, X.; Laliberte, J.; Huang, X.; Frei, H. Effect of wire and arc additive manufacturing (WAAM) process parameters on bead geometry and microstructure. *Addit. Manuf.* **2019**, *26*, 138–146. [CrossRef]
17. Huang, W.; Chen, S.; Xiao, J.; Jiang, X.; Jia, Y. Laser wire-feed metal additive manufacturing of the Al alloy. *Opt. Laser Technol.* **2021**, *134*, 106627. [CrossRef]
18. Liu, F.; Ji, S.S.; Shi, T.; Wan, L.; Shi, S.H.; Fu, G.Y. Parametric study of the three-beam laser inside coaxial wire feeding additive manufacturing. *Int. J. Adv. Manuf. Technol.* **2022**, *123*, 313–330. [CrossRef]
19. Mok, S.H.; Bi, G.; Folkes, J.; Pashby, I. Deposition of Ti–6Al–4V using a high power diode laser and wire, Part I: Investigation on the process characteristics. *Surf. Coat. Technol.* **2008**, *202*, 3933–3939. [CrossRef]
20. Moradi, M.; Hasani, A.; Pourmand, Z.; Lawrence, J. Direct laser metal deposition additive manufacturing of Inconel 718 superalloy: Statistical modelling and optimization by design of experiments. *Opt. Laser Technol.* **2021**, *144*, 107380. [CrossRef]
21. Ayed, A.; Bras, G.; Bernard, H.; Michaud, P.; Balcaen, Y.; Alexis, J. Additive manufacturing of Ti6Al4V with wire laser metal deposition process. *Mater. Sci. Forum* **2021**, *1016*, 24–29. [CrossRef]
22. Mbodj, N.G.; Abuabiah, M.; Plapper, P.; El Kandaoui, M.; Yaacoubi, S. Bead geometry prediction in laser-wire additive manufacturing process using machine learning: Case of study. *Appl. Sci.* **2021**, *11*, 11949. [CrossRef]
23. Liu, S.; Brice, C.; Zhang, X. Interrelated process-geometry-microstructure relationships for wire-feed laser additive manufacturing. *Mater. Today Commun.* **2022**, *31*, 103794. [CrossRef]
24. Zapata, A.; Bernauer, C.; Stadter, C.; Kolb, C.G.; Zaeh, M.F. Investigation on the cause-effect relationships between the process parameters and the resulting geometric properties for wire-based coaxial laser metal deposition. *Metals* **2022**, *12*, 455. [CrossRef]
25. Weidemann, T.; Abuabiah, M.; Shaqour, B.; Day, R.; Bergs, T.; Plapper, P. Influence on the Bead Geometry in Laser Metal Deposition with Wire. In Proceedings of the Lasers in Manufacturing Conference 2023, Munich, Germany, 26–29 June 2023

26. Amne Elahi, M.; Marozzi, A.; Plapper, P. Optimization of laser-assisted polypropylene aluminum joining. *Appl. Sci.* **2023**, *13*, 3582. [CrossRef]
27. Abioye, T.; Folkes, J.; Clare, A. A parametric study of Inconel 625 wire laser deposition. *J. Mater. Process. Technol.* **2013**, *213*, 2145–2151. [CrossRef]